

# From pressure fluctuations to dynamic loads on axisymmetric step flows with minimal number of kulites

S. Marié\*, S. Deck, P.E. Weiss

Office National d'Etudes et de Recherche Aéronautique 08 Rue des Vertugadins, FR-92190 MEUDON, France

## ARTICLE INFO

### Article history:

Received 26 January 2009  
Received in revised form 2 November 2009  
Accepted 3 December 2009  
Available online 13 December 2009

### Keywords:

Dynamic loads  
Pressure fluctuations  
Separating-reattaching flows  
Numerical simulations  
Experimental optimization  
Minimal number of kulites

## ABSTRACT

The present study focuses on two kinds of reconstruction methods designed to capture the dynamic loads acting on the reattaching part of an axisymmetric step flow. The pressure signals on discrete points of the geometry constitute the starting point of this study. Data are taken from a validated numerical simulation in order to maximize the number of sensors at the wall. First, an a priori methodology for the load reconstruction without any hypothesis on the flow behaviour is exposed. The influence of the number of sensors and their spatial distribution over the geometry is investigated. It is shown that azimuthal and longitudinal resolution have different effects on the reconstructed power spectral density of the load. Then, it is found that an experimental process with few unsteady sensors cannot provide an accurate prediction of the load. Then a second kind of reconstruction method based on the physical knowledge of the flow is presented. The original Nguyen approach initially developed for internal side loads is optimized with a spatial analysis and gives a satisfactory prediction of the load with only a minimal number of sensors.

© 2009 Elsevier Ltd. All rights reserved.

## 1. Introduction

### 1.1. Context

Separating–reattaching flows are the home of complex phenomena potentially involving loading on the reattaching part of the flow. In particular, during transonic flight, space launchers after-bodies are subjected to significant loads acting normally to the thrust. These dynamic loads (especially side loads) are caused by fluctuating pressure induced by a massively detached and turbulent flow. Thus, knowledge and control of side loads are of primary importance for the stability and integrity of launchers. Furthermore, the experimental process involves a wide range of measuring tools due to the diversity of the acting phenomena and the three-dimensional aspect of the flow. In practice, side loads are related to the pressure fluctuation but do not hold the same information. Indeed, pressure fluctuations are local data measured at a given point whereas dynamic loads are integral values relative to a given area. The different ways to get one from the other depends on both the measuring tools and the reconstruction methodology. This paper aims to develop such a method to get an accurate estimation of the load from the kulite information.

### 1.2. Measuring aerodynamic load

The survey of buffet loads and internal side loads have been the subject of numerous publications [1,18,19,25]. The load measurement problem highlighted in the literature [13] is found to be the same for our interest in external side loads. The main problem holds in the fact that the load measuring tools (accelerometer or mechanical balance) get the superposition of two different phenomena which are the aerodynamic load induced by the flow and the mechanical response of the structure. The first phenomenon is the direct effect of the reattaching turbulent flow and is the main interest of our study. The second phenomenon is characterized by the deformation of the structure and its inertial effects. Then, to distinguish quantitatively the impact of the aerodynamic load and the mechanical balance measurements, a special methodology has to be performed to subtract the inertial part of the load from the total measurement. This complex splitting technique has been applied in the past for side load estimation (see for example [13,26,2]). However, this kind of approach is very complex and demanding, and requires two different types of sensors: global sensors (mechanical balance) to get the overall loading and local sensors (accelerometers) for inertial corrections. In addition to these two kinds of sensors, the unsteady pressure sensors (kulites) used to characterize the pressure field around the structure could be mentioned. This approach then induces a heavy and complex experimental process.

\* Corresponding author. Present address: Centre National d'Etudes Spatiales – Rond Point de l'Espace, Courcouronnes 91023 EVRY CEDEX, France. Tel.: +33 1 60 87 71 14.

E-mail address: [simon.marie@cnes.fr](mailto:simon.marie@cnes.fr) (S. Marié).

Another way to get the aerodynamic load acting on the wall is to consider pressure fluctuations. Indeed, the dynamic load can be considered as a global effect of the overall fluctuating pressure field. The main advantage of such a method is the need for only one kind of device, the unsteady pressure sensors (kulites) which could be used for both load reconstruction and flow analysis. However, the main difficulty is to get global information (the load) from a local source (the pressure). Indeed, this method supposes that local information is taken at many points to make the reconstruction consistent. This means that a relatively high number of sensors should be involved in the experiment. Historically, the pressure fluctuation measurement has been actively studied [3,5,4] but only a few authors studied the load reconstruction [12,7,17]. The number of sensors used in the experiments and their locations are determined by the model size. For example, Nave and Coffey [16] used around 46 kulites to study the internal side loads in 1973 on a full scaled nozzle model. Later, in 2007 Camussi et al. [4] used 32 kulites to get the wall pressure fluctuations on a 1/30-scale launcher model. Then in our scope of investigation based on external loads on axisymmetric separating–reattaching flows, the geometry of the model does not allow a high number of sensors and the experiments made on such configurations [10,11,15] do not have enough kulites to reconstruct the unsteady load.

### 1.3. General philosophy

Today, numerical simulations can give reliable and accurate results on three-dimensional and unsteady flows. Recently, some numerical simulations of axisymmetric step flows have been performed and validated [21,8]. The undeniable advantage of numerical simulation lies in its ability to provide a huge amount of information. So, the number of recorded probes (numerical kulites) could be as large as memory and mesh resolution permit. In the general context of nowadays fluid mechanics, numerical simulation should not be considered any more as an independent way of study but as a complementary tools for experimental approaches [20]. So the main philosophy adopted in this paper is to bring quantitative information to the experimental process with numerical simulations. This approach have been particularly developed in the past few years for the study of wind tunnel flow-fields [14,9]. Moreover, in the general context of separated–reattached flows, the advanced numerical post-processing presented in this study can be applied to a wide range of experimental investigations. Then, in the context of unsteady load reconstruction, this paper aims to use the simulation data to study the influence of the number of sensors on the load reconstruction.

### 1.4. Organisation of the paper

The paper is organised as follows: Section 2 is dedicated to the introduction of the test case. Section 3 presents an *a priori* reconstruction of the load. This section aims at reconstructing the dynamic load without any hypothesis on the flow behaviour and involves the influence of the number of sensors. Section 4 focuses on the spatial behaviour of the flow and builds an optimized reconstruction method with a minimal number of kulites.

## 2. Test case

The general configuration (see Fig. 1a) is an axisymmetric body of diameter  $D = 100$  mm extended by an emergence of smaller diameter and of finite downstream extension  $L$  such as  $L/D = 1.2$  which corresponds to the ratio of the Ariane 5 launcher. It is immersed into a high subsonic flow with a free stream Mach number of 0.702 leading to a Reynolds number based on the forebody

diameter  $D$ :  $Re_D \approx 1.1 \times 10^6$ . The experimental study on axisymmetric base flows has been carried out in the S3Ch continuous research wind tunnel of ONERA's Chalais Meudon center. The test section is square shaped, and the dimensions of the test chamber are  $0.78 \times 0.78$  m<sup>2</sup>. A detailed description of the experimental set-up, equipment, and results is given in [10,11,15].

The numerical simulation of the present axisymmetric turbulent separating/reattaching flow has been performed on a 12 million point grid over a duration of 0.2 s. The numerical scheme used is based on a finite volume formulation and the turbulence is modelled by a Zonal Detached Eddy Simulation (ZDES) approach [6]. A comprehensive description of this computation is provided in [23,22] and the main parameters of the simulation are reminded in Table 1. The simulation has provided a data set composed of the temporal pressure signals on the reattached part stored at each mesh point. It should be noted here that numerical data (numerical sensors) will refer throughout the following to the fluctuating pressure and the static part will not be considered. Hence, data are constituted by  $N_x = 171$  rings with  $N_\phi = 240$  sensors, i.e. a total of  $N_c = N_x \times N_\phi = 41,040$  sensors recorded every  $\Delta t_c = 2\Delta t$ .

In addition, the temporal load on the reattached part is directly integrated from fluxes during the simulation and recorded every  $\Delta t_F = 5\Delta t$ . This signal will be considered in the following as a reference for the reconstructed load.

The main characteristics of the instantaneous and time-averaged flowfield are briefly reminded in Fig. 1b (see Ref. [8] for a review of an axisymmetric separating/reattaching flow). The external flow expands at the separation edge and a low-pressure region is formed immediately downstream of the base, characterized by a low-speed recirculating flow region. A secondary vortex is also evidenced in the corner. Interaction between this recirculating region and the external flow occurs through the free shear mixing region. The snapshot of the instantaneous flow highlights the roll-up of azimuthal vortical structures which grow by pairing and are rapidly replaced by large structures developing as the shear layer approaches reattachment. The occurrence of three-dimensional pressure fluctuations on the body surface induces unsteady asymmetrical side loads which are of primary interest in this study.

## 3. From pressure to side load

An *a priori* way to get the load acting on the emergence from the pressure fluctuation is to sum the contribution  $p_i$  of each sensor on an elementary surface  $d\mathbf{S}_i$ :

$$\mathbf{F}(t) = \int_0^{2\pi} \int_0^L p(x, \phi, t) r(x) n dx d\phi \equiv \sum_{i=1}^{N_c} p_i(t) d\mathbf{S}_i \quad (1)$$

where  $L$  is the emergence length,  $\equiv$  denotes the equivalence in discrete space,  $N_c$  is the number of sensors,  $d\mathbf{S}_i$  are elementary surface vectors around the sensor and  $\mathbf{n}$  is the surface normal (see Fig. 2). For a more accurate physical description, the spectral information of the load must be computed from its temporal signal given in Eq. (1). To access the frequency distribution of the load, we can compute the one-sided power spectral density (PSD) defined by:

$$G_F(f) = \lim_{T \rightarrow \infty} \frac{2}{T} E[Y_F \cdot Y_F^*] \quad (2)$$

where  $E[\cdot]$  is the statistical expectation operator,  $T$  the duration of the time series,  $Y_F$  the Fourier transform of signal  $F(t)$  and  $Y_F^*$  its complex conjugate. In experimental process and especially in numerical simulations, the acquisition time  $T$  cannot be infinite and the limit of Eq. (2) must be replaced by an estimator. In signal processing theory, many estimators can be used to evaluate  $G_F(f)$ . In this study, we used the Welch estimator [24] based on time averaging over short modified periodograms. In the following, the

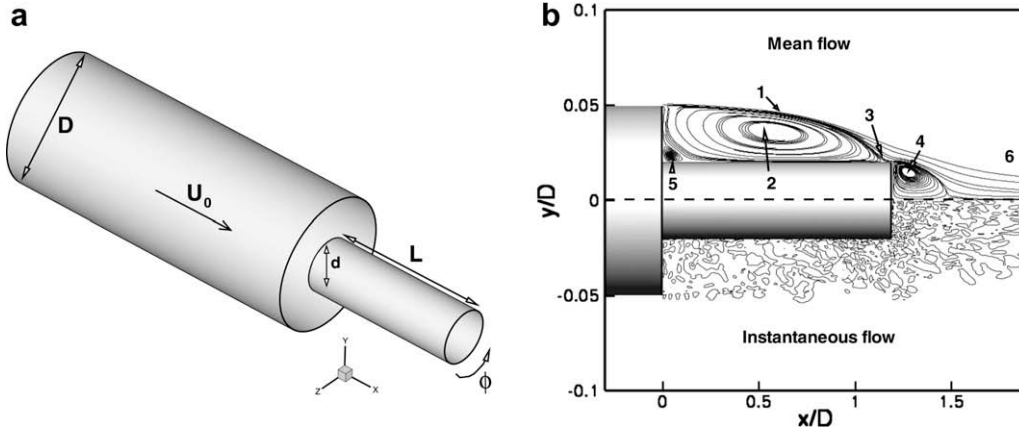


**Fig. 1.** (a) Sketch of the geometry.  $D = 0.1$  m,  $L = 1.2 D$ ,  $d = 0.4 D$  and  $U_0 = 237$  m/s. (b) Basic physics of the flow (upper part: streamlines in the mean field; lower part: Q criterion isocontours): 1. Mixing layer, 2. Recirculation area, 3. Reattachment point, 4. Second recirculation area, 5. Corner flow, 6. Turbulent wake.

**Table 1**  
Parameters of the simulation.

Mach	$P_0$ (Pa)	Simulation time (s)	$\Delta t$ (s)	$\Delta x_{min}$ (m)	$\Delta x_{max}$ (m)
0.702	72,440	0.2	$2 \times 10^{-6}$	$1.5 \times 10^{-4}$	$1.2 \times 10^{-3}$

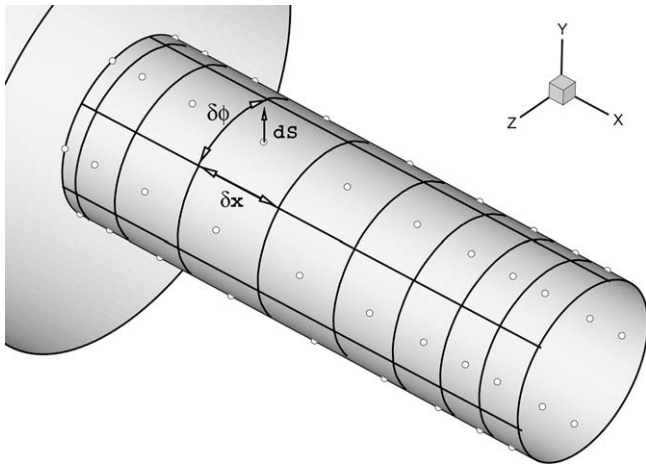


**Fig. 2.** Example of sensor distribution with  $N_x = 9$  and  $N_\phi = 6$ .

estimator will be designated by  $\hat{G}_F(f)$ . Then, a simple way to assess the side load from pressure fluctuation is to compute directly  $\hat{G}_F(f)$  from Eq. (2). This method only requires the temporal signal  $p(t)$  to get  $F(t)$  from Eq. (1). In numerical simulations, this signal can be easily obtained by direct integration of the pressures. However, from the experimental side and due to storage limitations, the temporal signal is often post-processed directly during acquisition and transformed into spectral data in the form of interspectral matrix. Therefore, Eq. (2) must be rewritten. Thus, as the Fourier transform is a linear operation, Eqs. (1) and (2) yield:

$$\hat{G}_F(f) = \lim_{T \rightarrow \infty} \frac{2}{T} E \left[ \sum_{i=1}^{N_c} \sum_{j=1}^{N_c} Y_{p_i} Y_{p_j}^* \mathbf{dS}_i \mathbf{dS}_j \right] \quad (3)$$

where  $Y_{p_i}$  is the Fourier transform of  $p_i(t)$ . Finally, we can write:

$$\hat{G}_F(f) = \sum_{i=1}^{N_c} \sum_{j=1}^{N_c} \hat{G}_{ij}(f) \mathbf{dS}_i \mathbf{dS}_j \quad (4)$$

where  $\hat{G}_{ij}(f)$  is the interspectral matrix estimator. The use of Eq. (4) does not require the knowledge of the temporal signal but only the

interspectral matrix and is thus more convenient for experimental data analysis.

It is important to note that Eq. (2) with the Welch estimator and Eq. (4) are completely equivalent. Historically, only Eq. (4) was used to analyse experimental data. We can now wonder, which method is more interesting in terms of computational cost. Table 2 indicates the number of operation used by each method. The first row is related to Eq. (2) which could only be used with the temporal signal. The second row is related to Eq. (4) which could be evaluated directly with the interspectral matrix (second column) or with the temporal signal by reconstructing the interspectral matrix with the Welch interspectral procedure (first column).

It becomes obvious that using Eq. (4) with temporal signal is the worst solution because  $\frac{N_s^2}{2} N_{wxy} \gg N_c N_w$ . Likewise, it can be found in [24] that  $N_w = \mathcal{O}(n \log L)$  where  $n$  is the signal length and  $L$  the length of a block. Thus, Eq. (2) with the temporal signal is faster than Eq. (4) with the interspectral matrix only if  $N_c > \frac{2}{3} n \log L$ . Practically, this condition is never satisfied because the number of sensors is never so high. However, it should be noticed that  $N_s$  does not take into account the post-processing time spent in the acquisition process. Moreover, in numerical simulations, we cannot afford to do the post-processing during the simulation for CPU reasons. In this study based on numerical simulations, we will use Eq. (2) with temporal signal to evaluate the load PSD from pressure fluctuations.

### 3.1. Surfaces projection

To assess the load from Eq. (2), the elementary surface vector  $\mathbf{dS}$  must be computed. In a general way, this vector can be expressed by splitting the whole surface into elementary ones surrounding each sensor. Thus, we can write:

$$\mathbf{dS} = \begin{pmatrix} \frac{\delta\phi}{2} (r_2^2 - r_1^2) \\ \delta\phi \delta x \bar{r} \cos \phi \\ \delta\phi \delta x \bar{r} \sin \phi \end{pmatrix}$$

**Table 2**

Number of floating point operations used for each method.  $N_c$  is the number of sensors used,  $N_w$  is the number of operations used during the Welch procedure [24] and  $N_{wxy}$  the number of operations for the Welch interspectral procedure.

Method/data used	Temporal signal	Interspectral matrix
Eq. (2)	$\mathcal{O}(N_c N_w)$	$\times$
Eq. (4)	$\mathcal{O}\left(\frac{N_s^2}{2} N_{wxy}\right)$	$N_s = \mathcal{O}\left(\frac{2}{3} N_c^2\right)$

where  $r_1$  and  $r_2$  are the bottom and top radius of each surface ring respectively and  $\bar{r} = (r_1 + r_2)/2$ . In the case of a cylinder, we have  $r_1 = r_2$  and the surface vector reduces to:

$$d\mathbf{S}_i = \begin{pmatrix} 0 \\ \frac{2\pi}{N_\phi} h_i R \cos \phi_i \\ \frac{2\pi}{N_\phi} h_i R \sin \phi_i \end{pmatrix}$$

where  $N_\phi$  is the number of sensor on a ring,  $h_i$  the height of a ring and  $R$  is the cylinder radius. Fig. 2 shows an example of the sensor distribution with the surface elements surrounding the sensors on the emergence.

### 3.2. Validation with all sensors

To validate the approach presented above, Fig. 3 compares the one-sided load PSD  $G(f)$  on the emergence, computed with Eq. (2) and the reference obtained by integration during the simulation. The Welch estimator is used with 31 blocks with 50% overlapping and a frequency resolution of 80 Hz. For the representation, we plot the  $f \cdot G(f)$  quantity function of the non dimensional Strouhal number  $St_D = f \cdot D/U_\infty$  in the logarithmic scale. This representation conserves the rms value:

$$G_{rms} = \int_0^\infty G(f) \cdot df = \int_0^\infty f \cdot G(f) \cdot d(\log f)$$

First, one can notice that the reconstructed spectra compares well with the reference. The energy ratio  $\frac{\sigma_{rec}}{\sigma_{ref}}$  is equal to 1.0093 for Y-axis load and 1.0012 for Z-axis load. From a physical point of view, as highlighted by Deck and Thorigny [8], the load is dominated by a peak around  $St_D = 0.2$  which contains most of the energy spectrum. This peak can be attributed to the shedding phenomenon signature. This physical description will be further detailed in the following and will help us to reduce the number of sensor for the reconstruction in the second part of this study.

### 3.3. Influence of sensor distribution

In this section, we explore the influence of the sensor distribution on the load reconstruction. The underlying objective is to reduce the number of sensors to see the influence on the reconstructed PSD. To improve our understanding of the distribution influence, the azimuthal and longitudinal location will be studied separately. The reconstructed load will be plotted for different values of the couple  $N_x-N_\phi$ , in which  $N_x$  is the number of rings and  $N_\phi$  is the number of sensors on a ring. In this part of

the study, we do not make any hypothesis on the spatial distribution of the load, thus we choose a uniform distribution of the rings across the body such that each ring has the same height:  $h_i = L/N_x$ , with  $L$  the length of the reattached part. Moreover, this approach implies that the pressure sensor  $p_i$  has to be constant on the elementary surface  $d\mathbf{S}_i$ . This hypothesis is as strong as elementary surfaces are large, which is the case when the number of sensors is low.

#### 3.3.1. Longitudinal distribution

To see the influence of the longitudinal distribution (number of rings), we set the number of sensors on a ring to  $N_\phi = 24$  which corresponds to 10% of the total azimuthal number and change the number of rings ( $N_x = 15$ ,  $N_x = 40$  and  $N_x = 171$ ). Fig. 4 shows the evolution of the reconstructed load with the number of rings.

First, one can note that both curves are still close to the reference. In the worst case, we reduce the total number of sensors to 360 keeping relatively good qualitative results. However, the peak around  $St_D = 0.2$  is overestimated for the y-load and underestimated for the z-load. Likewise, we observe an overestimation of high frequencies ( $St_D \geq 1$ ) when the number of rings decreases. Generally, we see in this case that reducing the amount of information (i.e. the number of sensors) still allows an accurate estimation of the load.

#### 3.3.2. Azimuthal distribution

Let us now investigate the influence of the azimuthal distribution on the reconstructed pressure load. To this end, we choose a given number of rings ( $N_x = 15$  which corresponds to approximately 10% of the total longitudinal number) and assess the influence of the  $N_\phi$  parameter. As an example, Fig. 5 shows the reconstructed load for three different values of this parameter.

The same phenomenon than for longitudinal distribution is observed. However, the overestimation at high frequencies seems to be more important in this case. This may appear surprising because of the axisymmetrical geometry. Indeed, for this type of geometry, one can expect a uniform pressure distribution in the azimuthal direction. Thus, this behaviour could be the signature of a structured and asymmetric flow in the azimuthal direction. These types of considerations will be further explored in Section 4.2.

#### 3.3.3. Reconstruction with few sensors

Now, we reduce the information to a few number of sensors ( $N_c \leq 100$ ) to see how the load reconstruction behaves. This few number of sensor corresponds to those involved in most of the experimental processes. It is shown in Fig. 6 that a few sensors

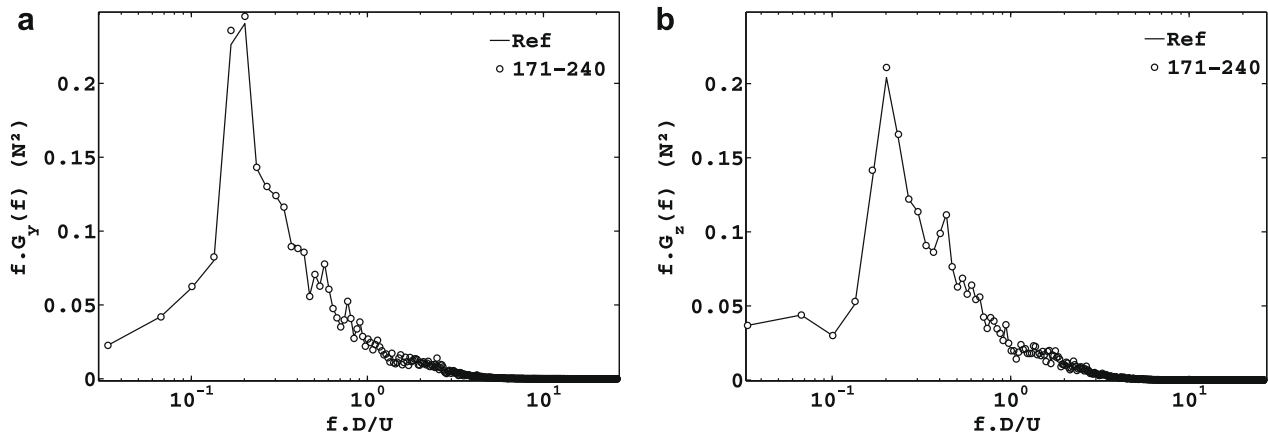


Fig. 3. (○) Load spectra reconstructed from the pressure fluctuation with Eq. (2) with the complete sensor set:  $N_x = 171$  and  $N_\phi = 240$ . (—) reference load spectra integrated during the simulation. (a) Load on y. (b) Load on z.

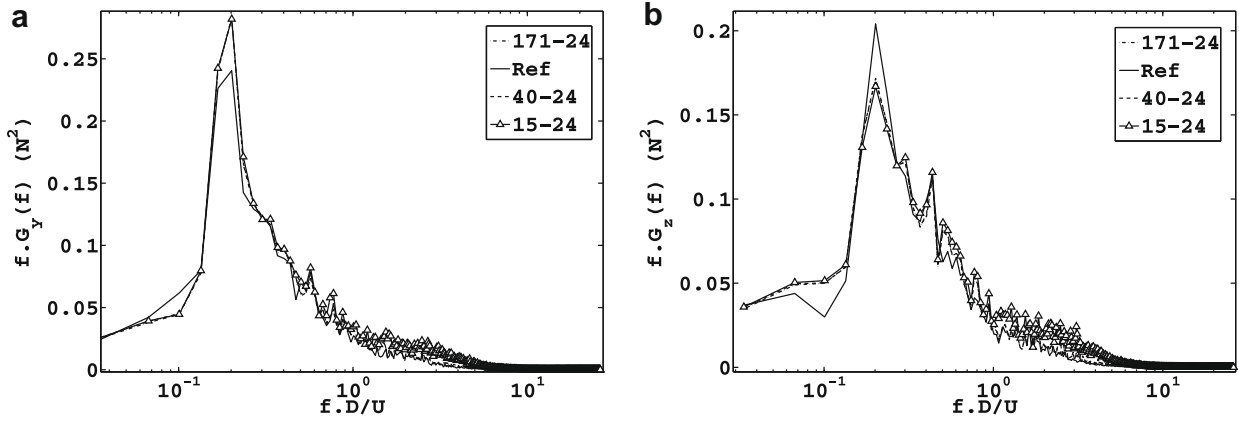


Fig. 4. Load spectra reconstructed with different numbers of rings in the longitudinal direction. Each ring has  $N_\phi = 24$  sensors.

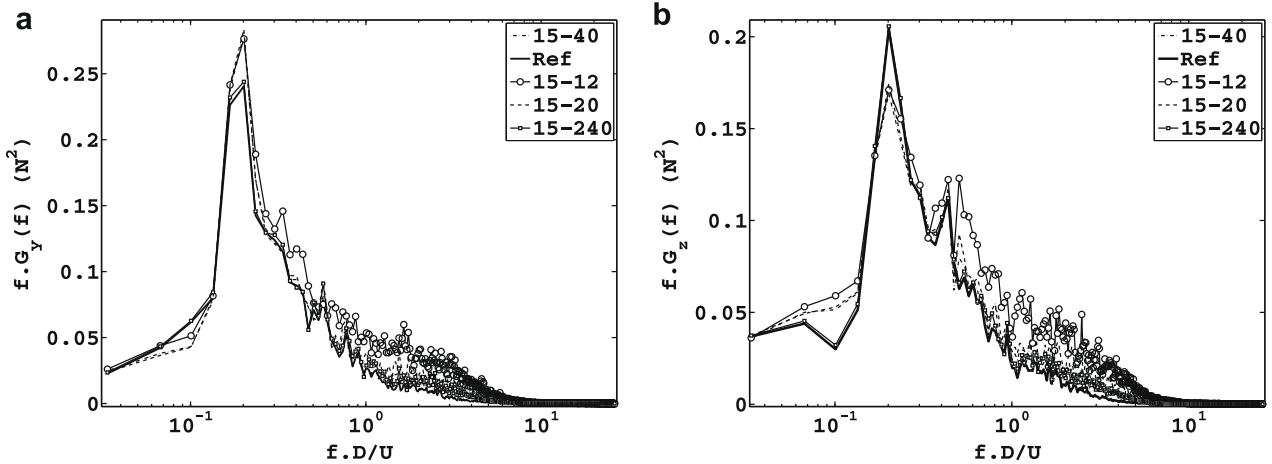


Fig. 5. Load spectra reconstructed with different numbers of sensors on a ring in the azimuthal direction. Here  $N_x = 15$  rings are used.

could lead to non-physical results. Indeed, if a peak at  $St_D = 0.2$  occurs, the global frequency distribution of the load is not conserved when the number of sensors becomes small ( $N_c = 15$ ).

Generally, an overestimation of the load is observed when few sensors are used. This is a consequence of the surface increase around each sensors. The reconstruction method assesses that the pressure phase is the same on an elementary surface. So, if

the elementary surface increases, the pressure phase is supposed to be constant on a larger area which leads to an overestimation of the load.

This could become very problematic for experimental processes where the number of sensors should be limited due to bulk constraints of the model. A practical example is given in Fig. 7, where the same number of sensors with a different distribution could

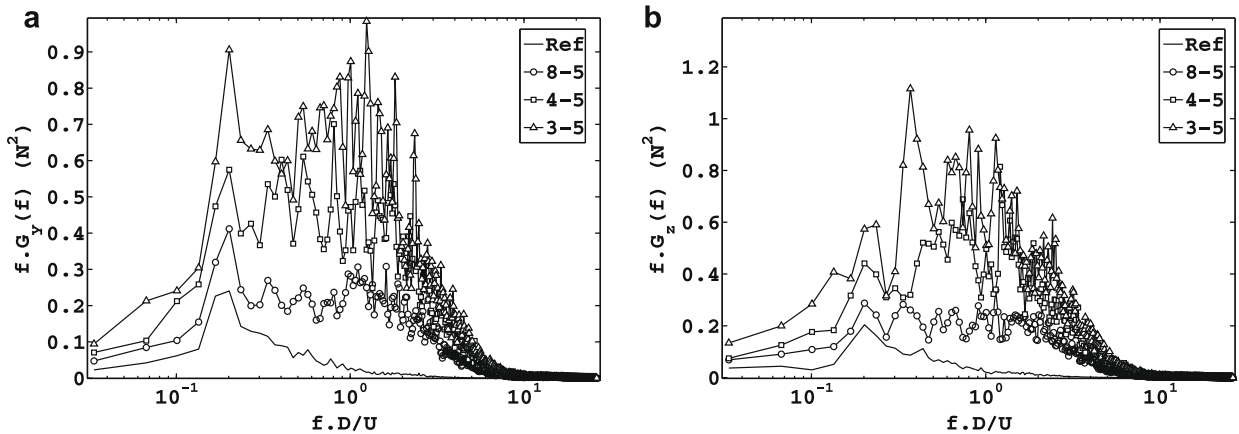


Fig. 6. Load spectra reconstructed with 40, 20 and 15 sensors.

lead to different results. This highlights the interest of numerical computations which can inform experimentalists about the best location for the sensors.

### 3.4. The global criteria

In order to quantify the compromise between the number of sensors and the error on the reconstructed load, a global criteria should be defined. The following definition is adopted:

$$C = N_c \left\langle \left| 1 - \frac{G_{rec}(f)}{G_{ref}(f)} \right|^2 \right\rangle \quad (5)$$

where  $N_c$  is the total number of sensors used,  $G_{rec}$  is the PSD of the reconstructed load,  $G_{ref}$  the PSD of the reference and  $\langle \cdot \rangle$  denotes the frequency averaging. The quadratic value of the frequency averaging is chosen to highlight the error importance. Indeed, even if the number of sensors is weak, the quadratic error will enhance the criteria value. Then, the smaller the criteria the better the compromise between reconstruction quality and the number of sensors. Table 3 gives a range indication for the representative values of the criteria applied on the reconstruction of Figs. 4–7.

The criteria is spread over a wide range of values. However, attention must be focussed on the  $C_{peak}$  criteria which corresponds to the most energetic frequency range. The value of 250 for the 3–5 configuration denotes the large error committed on the reconstructed load when few sensors are used. Furthermore, it can be seen that the minimal value of  $C_{peak}$  is obtained for the 15–20 configuration which corresponds to the best compromise between the number of sensors and the error committed on the reconstructed load. However the number of sensors of this configuration ( $15 \times 20 = 300$ ) remains relatively high for an experiment. So a better approach should be found for the reconstruction by taking the physical behaviour into account.

This analysis of the reconstructed load has evidenced the significance of the spatial distribution in the choice of sensors. Moreover, we can ask if the accuracy of this analysis could be improved by coupling the topology of the flow with its physical behaviour. Thus, a detailed analysis of the flow should be performed to optimize the distribution of sensors for quantitative reconstruction of the load.

## 4. Physical and optimized reconstruction

### 4.1. The Nguyen approach: the $m = 1$ antisymmetric mode

The flow behaviour inside the nozzle is quite different than outside but involves some similar phenomena. In the past few

**Table 3**

Values of the global criteria  $C$  for different values of  $[N_x, N_\theta]$ .  $C_{tot}$  takes into account the whole frequency range whereas  $C_{peak}$  takes only into account the energy contained around the peak  $St_D \approx 0.2$  ( $0 \leq St_D \leq 0.5$ ).

$N_x - N_\theta$	171–240	15–20	8–5	3–5
$C_{tot}$	15	6430	$1.3 \times 10^4$	$1.2 \times 10^5$
$C_{peak}$	9	6	44	250

years, many authors got interested in the dynamics of internal side loads. For instance, Nguyen has shown [17] that the internal side loads could be reconstructed from two opposite lines of sensors. The main idea of this model was to assume that the forces acting on the nozzle area were principally generated by the antisymmetry of the reattachment region which could be characterized by the antisymmetric  $m = 1$  mode of the internal flow. It has been emphasized [8] that a similar antisymmetric mode was partially responsible for the external side loads. So, in a preliminary phase, the idea is to see if the approach proposed by Deck and Nguyen [7] for internal flow can be applied on external flow.

The main idea of the Nguyen approach is to isolate mathematically the effects of the antisymmetric mode. This is made possible by considering the mean pressure along two diametrically opposite lines. The mean pressure along a line of sensors is obtained by integrating the wall pressure  $p(x, \phi, t)$  along  $x$ :

$$\bar{p}(\phi, t) = \frac{1}{L} \int_0^L p(x, \phi, t) r(x) dx \quad (6)$$

where  $L$  and  $r(x)$  denote respectively the length of integration and the evolution of the body radius in the streamwise direction. For this study, this radius is set to the constant  $R = d/2 = 0.02$  (see Fig. 1b). Let  $\bar{p}_{\phi_0}(t)$  and  $\bar{p}_{\phi_1}(t)$  (with  $\phi_1 = \phi_0 + \pi$ ) be the time series of two opposed lines: the Nguyen model extracts the mathematical signature of the  $m = 1$  mode in the first coefficient of the Fourier series decomposition of vector  $[\bar{p}_{\phi_0}(t), \bar{p}_{\phi_1}(t)]$ . The fluctuating pressure field, being a periodic function of the azimuthal angle  $\phi$ , can be expanded in Fourier series as follows:

$$\bar{p}(\phi, t) = a_0 + \sum_{k=1}^{\infty} [a_k(t) \cos(k\phi) + b_k(t) \sin(k\phi)] \quad (7)$$

with

$$\begin{cases} a_1(t) = \frac{1}{2\pi} \int_0^{2\pi} \bar{p}(\phi, t) \cos(\phi) d\phi \\ b_1(t) = \frac{1}{2\pi} \int_0^{2\pi} \bar{p}(\phi, t) \sin(\phi) d\phi \end{cases} \quad (8)$$

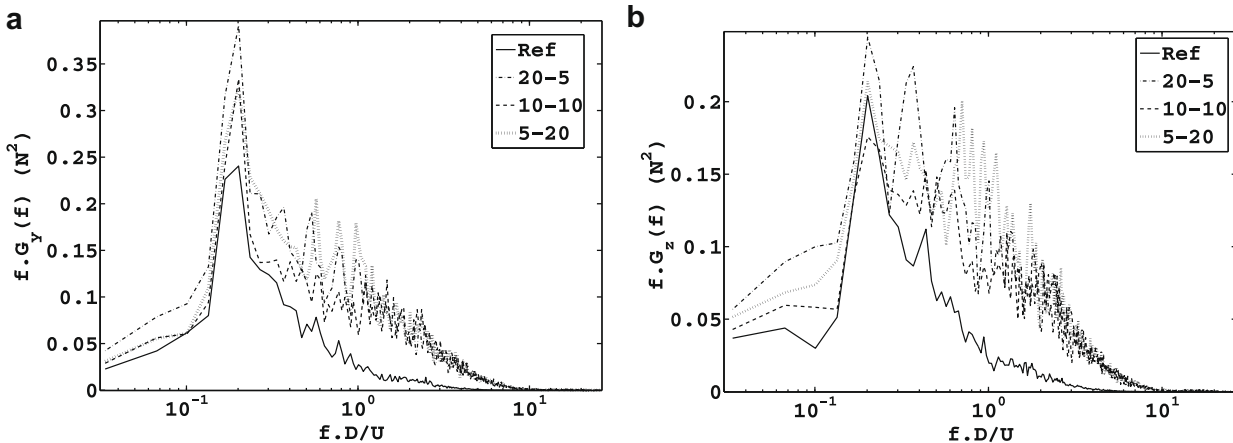


**Fig. 7.** Load spectra reconstructed with 100 sensors with different distribution.

This coefficient can be easily computed in discrete form. Thus, for the vector  $[\bar{p}_{\phi_0}(t), \bar{p}_{\phi_1}(t)]$ , the  $a_1(t)$  coefficient could be written in the form:

$$\begin{cases} a_1(t) = \frac{1}{2} [\bar{p}_{\phi_0}(t) \cos(\phi_0) + \bar{p}_{\phi_1}(t) \cos(\phi_1)] \\ b_1(t) = \frac{1}{2} [\bar{p}_{\phi_0}(t) \sin(\phi_0) + \bar{p}_{\phi_1}(t) \sin(\phi_1)] \end{cases} \quad (9)$$

Then one can note that, substituting Eq. (6) in Eq. (1) gives:

$$\begin{cases} Fy(t) = L^2 \int_0^{2\pi} \bar{p}(\phi, t) \cos \phi d\phi \\ Fz(t) = L^2 \int_0^{2\pi} \bar{p}(\phi, t) \sin \phi d\phi \end{cases} \quad (10)$$

The main hypothesis of the Nguyen model is to consider that the mean pressure  $\bar{p}(\phi, t)$  is dominated by  $a_1(t)$ . Thus the PSD of the load given in Eq. (2) could be rewritten using Eq. (10):

$$\begin{cases} G_{Fy}(f) = L^4 \pi^4 G_{a_1}(f) \\ G_{Fz}(f) = L^4 \pi^4 G_{b_1}(f) \end{cases} \quad (11)$$

where  $G_{a_1}(f)$  and  $G_{b_1}(f)$  are respectively the PSD of coefficients  $a_1$  and  $b_1$ . This model was validated in [7] for internal nozzle side loads computed with unsteady pressure data issued from both experiment and numerical simulation.

Fig. 8 presents the model predictions for external buffet loads on the y-axis and z-axis of our configuration. It is made obvious

that the PSD level is clearly overestimated by the model especially at high frequencies.

These results show that the hypothesis assuming the averaged pressure field on the emergence  $\bar{P}(\phi, t)$  is dominated by the first mode is too crude. An analysis of the spatial organisation of the fluctuating pressure field appears to be necessary.

#### 4.2. Spatial organisation of the fluctuating pressure field

The purpose of this section is to get a better understanding of the spatial organisation of the antisymmetric pressure mode acting on the wall. Indeed, it has been found that the basic Nguyen model, initially developed for internal side loads, was not adapted for external predictions. Hence, let us consider the coherence function between two signals  $x$  and  $y$  defined by:

$$\gamma_{xy}(f) = \frac{G_{xy}(f)}{\sqrt{G_x(f)G_y(f)}} \quad (12)$$

where  $G_{xy}$  represents the one-sided cross-spectral density of signal  $x$  and  $y$ . To analyse the  $m = 1$  mode, it is worth getting interested in the coherence  $\gamma_{x_0x_1}$  between a sensor located at  $(x_0, \phi_0)$  and a sensor located at  $(x_1, \phi_1)$  with  $\phi_1 = \phi_0 + \pi$ . This coherence thus depends on four variables and we have  $\gamma_{x_0x_1} = \gamma_{x_0x_1}(x_0, x_1, \phi_0, St)$  where  $St_D = f \cdot D/U_\infty$  denotes the Strouhal number. For the purpose of

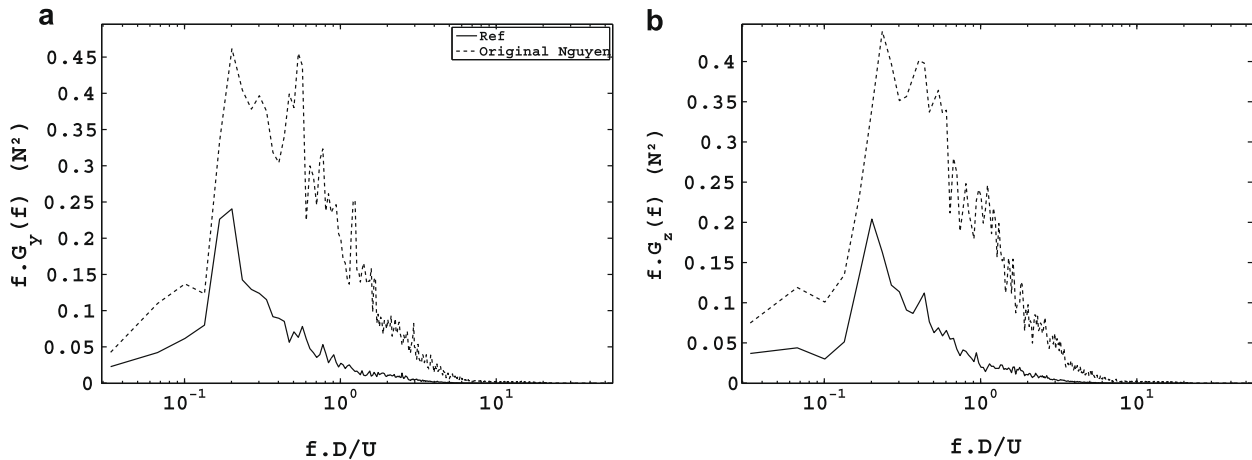


Fig. 8. Comparison between reference PSD and reconstructed PSD with Nguyen model on y-axis (a) and z-axis (b).

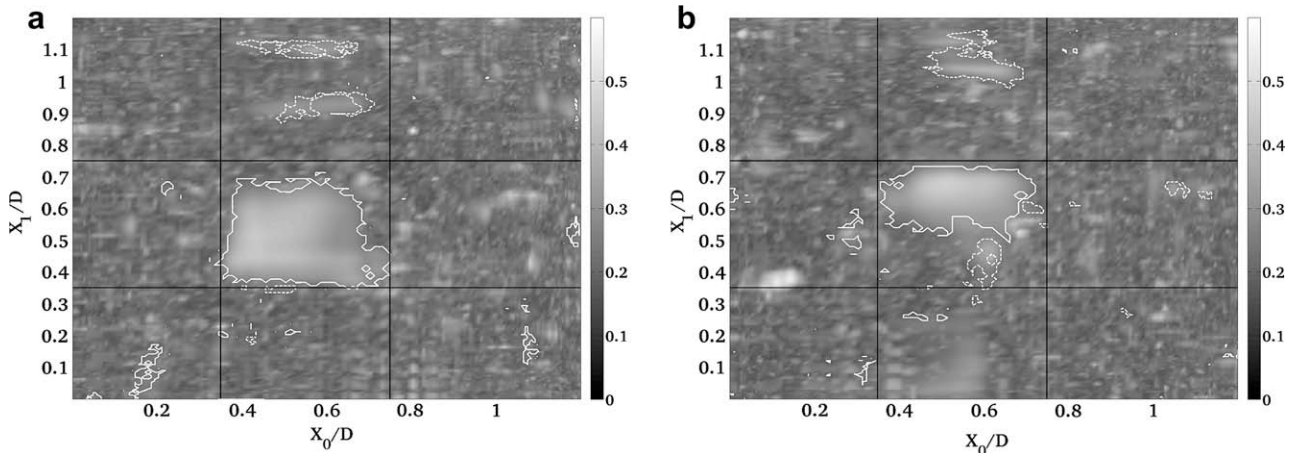
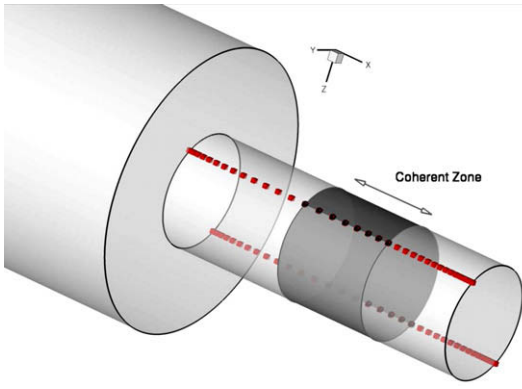


Fig. 9. Modulus of the maximum square coherence ( $\gamma^2$ ) for two opposite lines diametrically opposed with (a)  $\phi_0 = 0$  and (b)  $\phi_0 = \pi/2$ . Filled contours represent the  $Str_0 = 0.2$  locations with phase  $\theta \geq 3\pi/4$  and dashed contours with phase  $\theta \leq \pi/10$ .



**Fig. 10.** Sensor distribution for the original (red cubes) and optimized (black spheres) Nguyen model. (For interpretation of the references to colour in this figure legend, the reader is referred to the web version of this article.)

**Table 4**

Values of the global criteria  $C$  for different values of  $N_x$ .  $C_{peak}$  takes into account only the energy contained around the peak ( $0 \leq St \leq 0.5$ ).

$N_x$	35	18	7	5	2
$C_{tot}$	76	38	75	73	23
$C_{peak}$	7.8	4.7	3.9	4.3	4.6

understanding the antisymmetric mode, the frequency domain could be reduced to the locus of the maximum coherence, i.e.  $\gamma_{x_0 x_1} = \gamma_{x_0 x_1}(x_0, x_1, \phi_0, St_0)$  where  $St_0$  represents the Strouhal number where the maximum occurs.

Since  $\gamma_{x_0 x_1}$  is a complex value, it can be represented by its modulus  $|\gamma_{x_0 x_1}|$  and its phase  $\theta$ . As the antisymmetric mode is characterized by a phase close to  $\pi$  (phase in opposition), we focus on the part of the coherence which has a phase close to  $\pi$ . Fig. 9 is the representation of  $\gamma_{x_0 x_1}(x_0, x_1, \phi_0 = 0, St_0 = 0.2)$  and  $\gamma_{x_0 x_1}(x_0, x_1, \phi_0 = \pi/2, St_0 = 0.2)$ . We have superimposed onto the coherence shape, the contour of  $St_0$  in filled lines when the phase  $\theta$  is close to  $\pi$  and in dashed lines when  $\theta$  is close to zero. A high coherence zone located between  $x/D = 0.35$  and  $x/D = 0.75$  is highlighted. More precisely, it is characterized by a high coherence and an opposite phase at  $St_0 = 0.2$ . This coherent zone is reminiscent to the absolute unstable flow region suggested in [8] and demonstrated in [22]. For our study, we will demonstrate that this zone plays a crucial role for the reconstruction of side loads. Indeed, the occurrence of this particular zone is the direct

explanation of the unsuccessful basic Nguyen model which consider the antisymmetric mode present along the small cylinder length. Then the Nguyen model can be revisited by considering the influence of this coherent zone.

#### 4.3. A space-optimized Nguyen approach

The basic Nguyen model considers the whole length of the small cylinder to calculate the mean pressure  $\bar{p}$  (see Eq. (6)). This supposes a relatively uniform evolution of the antisymmetric mode along the cylinder length. It has been shown in the previous section that this mode is particularly active in a localized region  $[x_{inf}, x_{sup}]$ . The idea is thus to restrict the averaging only to this zone. Then Eq. (6) becomes:

$$\check{\bar{p}}(\phi, t) = \frac{1}{\check{L}^2} \int_{x_{inf}}^{x_{sup}} p(x, \phi, t) r(x) dx \quad (13)$$

where  $\check{L} = x_{sup} - x_{inf}$ . In the same way, the new coefficients defined in Eq. (9) becomes:

$$\check{a}_1(t) = \frac{1}{2} [\check{\bar{p}}_{\phi_0}(t) \cos(\phi_1) + \check{\bar{p}}_{\phi_1}(t) \cos(\phi_0)] \quad (14)$$

These coefficients describe the occurrence of the antisymmetric mode in the coherent region. Finally, the PSD of the load for this space-optimized model becomes:

$$G_{Fy}(f) = \check{L}^4 \pi^4 G_{\check{a}_1}(f) \quad (15)$$

In Fig. 10, we can see the sensor distribution for the original Nguyen model (red cubes). This distribution takes into account all the sensors available on the emergence length. For the optimized model, the sensor distribution takes only into account the length of the coherent zone (black spheres). In order to completely optimize the distribution, we can consider only some of the sensors along the coherent zone and look for an optimized distribution by evaluating the global criteria (5) defined in Section 3.4 for each reconstruction. The results are exposed in Table 4. It is shown that the minimum value of the  $C_{peak}$  criteria is reached for seven points along the coherent zone. The corresponding reconstruction is shown in Fig. 11.

The level and the frequency distribution of the reconstructed load are in good agreement with the reference. Moreover, to obtain these results, only seven sensors along a line of the coherent zone were used which corresponds to 28 total sensors ( $N_\phi = 4$  to get the y-axis and z-axis load and  $N_x = 7$ ). If we focus on the spectral

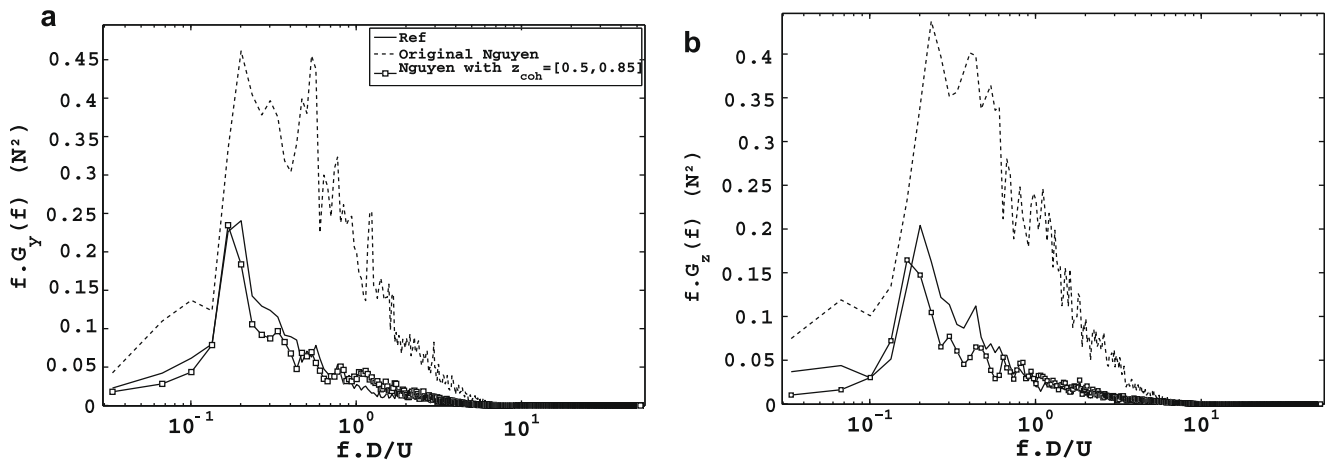


**Fig. 11.** Comparison between reference PSD and reconstructed PSD with spatially optimized Nguyen model.

energy predicted by the reconstruction, the ratio between the reference rms value and the reconstructed one is around 0.15. By comparing the results gathered in Tables 3 and 4, it is shown that the space-optimized model decreases considerably the global criteria values and so enhances the efficiency of the reconstruction.

Finally, it has been shown that the driver responsible for the external side loads can be attributed to an antisymmetric mode confined in a particular area which could be the only area considered for the choice of sensor location. These considerations are now compatible with an experimental investigation and could be taken into account for future experiments.

## 5. Conclusion

This study has used numerical simulation data to highlight the importance of sensor distribution for dynamic load reconstruction in experimental processes. The use of kulites for load studies is motivated by the deficiencies and complexities of classical experimental tools for unsteady load measurements. The large array of data computed by the simulation led to an accurate study of the sensor distribution. First, it has been shown that a weak resolution of sensors in the azimuthal direction led to an overestimation at high frequencies of the reconstructed load. Then it has been highlighted that an *a priori* reconstruction with few sensors induced a non-physical prediction of the dynamic load. These weaknesses are due to the incompatibility between evenly distributed sensors and the study of a spatially structured flow. Indeed, in the second part of the study, the spatial analysis of the pressure correlation has shown that the shedding phenomenon involved in axisymmetric flow was particularly active in a confined area. Then, with this accurate knowledge brought by numerical simulations, an optimized reconstruction method has been built by taking into account the physical behaviour of the flow. This method gives satisfactory results with 28 sensors and exhibits a 15% errors on the rms values which remains acceptable for a reconstruction method based on only one kind of sensors.

These results show that numerical simulations can be a powerful and complementary tool for experimental processes and could be used for experimental optimization which aims to provide the maximum knowledge with a minimum amount of information.

## References

- [1] Alziary de Roquefort T. Unsteadiness and side loads in over-expanded supersonic nozzles. In: Fourth European symposium on aerothermodynamics for space vehicles, Capua, Italy, October 2001. ESA.
- [2] Baban F, So RMC, Ötügen MV. Unsteady forces on circular cylinders in a cross-flow. *Exp Fluids* 1989;7:293–302.
- [3] Bull WK. Wall-pressure fluctuations beneath turbulent boundary layers: some reflections on forty years of research. *J Sound Vib* 1996;3(190):299–315.
- [4] Camussi R, Guj G, Imperator B, Pizzicaroli A, Perigo D. Wall pressure fluctuations induced by transonic boundary layers on a launcher model. *Aerosp Sci Technol* 2007;11:349–59.
- [5] Chun S, Liu YZ, Sung HJ. Wall pressure fluctuations of a turbulent separated and reattaching flow affected by an unsteady wake. *Exp Fluids* 2004;37(4).
- [6] Deck S. Zonal-detached-eddy-simulation of the flow around a high-lift configuration. *AIAA J* 2005;43(11):2372–84.
- [7] Deck S, Nguyen AT. Unsteady side-loads in a thrust-optimized contour nozzle at hysteresis regime. *AIAA J* 2004;42(9):1878–88.
- [8] Deck S, Thorigny P. Unsteadiness of an axisymmetric separating–reattaching flow. *Phys Fluids* 2007;19:065103.
- [9] Deese JE, Johnson JG, Agarwal AK, Soni BK, Crites RG, Rueger ML. Simulation of wind tunnel flowfields. *AIAA-paper*, Reno; 1992.
- [10] Deprés D. Analyse physique et modélisation des instationnarités dans les écoulements d'arrière-corps transsoniques. PhD thesis, Université de la Méditerranée: Aix-Marseille II; 2003.
- [11] Deprés D, Reijasse P, Dussauge JP. Analysis of unsteadiness in afterbody transonic flows. *AIAA J* 2004;42(12):2341–550.
- [12] Dumnov GE. Unsteady side-loads acting on the nozzle with developed separation zone. *AIAA-paper*, 96-3220; 1996.
- [13] Garçon F, Drevet JP. Unsteady load measurements on the main engine nozzle of the Ariane 5 launch vehicle. In: Third European symposium on aerothermodynamics for space vehicles ESA. Noordwijk, The Netherlands: ESTEC; December 1998, p. 623.
- [14] Melber-Wilkending S et al. A new approach in CFD supported wind tunnel testing. In: 25th International congress of the aeronautical sciences; 2006.
- [15] Meliga P, Reijasse P. Unsteady transonic flow behind an axisymmetric body equipped with two boosters. *AIAA paper*, 2007-4564; 2007.
- [16] Nave LH, Coffey GA. Sea level side loads in high area ratio rocket engines. In: *AIAA/SAE 9th propulsion conference*, number 73-1284, AIAA, Las Vegas, Nevada, November 5–7, 1973.
- [17] Nguyen AT. Décollement instationnaire et charges latérales dans les tuyères propulsives. PhD thesis, Université de Poitiers; 2003.
- [18] Ragab MM. Buffet loads prediction for a launch vehicle and comparison to flight data. *J Spacecraft Rockets* 1992;29(6).
- [19] Rainey AG. Progress on the launch vehicle buffeting problem. *J Spacecraft Rockets* 1965;2(3).
- [20] Sagaut P, Deck S. Large eddy simulation for aerodynamics: status and perspective. *Philos Trans Roy Soc A* 2009;367(June):2849–60.
- [21] Simon F, Deck S, Guillen Ph, Sagaut P, Merlen A. Numerical simulation of the compressible mixing layer past an axisymmetric trailing edge. *J Fluid Mech* 2007;591(November):215–53.
- [22] Weiss PE, Deck S, Robinet JC, Sagaut P. On the dynamics of axisymmetric turbulent separating/reattaching flows. *Phys Fluids* 2009;21:075103.
- [23] Weiss PE, Deck S, Sagaut P. Zonal-detached-eddy-simulation of a two-dimensional and axisymmetric separating/reattaching flow. *AIAA paper* 2008-4377; 2008.
- [24] Welch PD. The use of fast Fourier transform for the estimation of power spectra: a method based on time averaging over short modified periodograms. *IEEE Trans Audio Electroacoust* 1967;AU-15(2):70–3.
- [25] Wong H, Meijer J, Schwane R. Experimental and theoretical investigation of base-flow buffeting on Ariane 5 launch vehicles. *J Propul Power* 2007;23(1):116–22.
- [26] Zhang HJ, Huang L, Zhou Y. Aerodynamic loading on a cylinder behind airfoil. *Exp Fluids* 2005;38(5).